UC Irvine
UC Irvine Previously Published Works

Title

MicroRNA-processing Enzymes Are Essential for Survival and Function of Mature Retinal Pigmented Epithelial Cells in Mice.

Permalink

https://escholarship.org/uc/item/393339jh

Journal

Journal of Biological Chemistry, 292(8)

Authors

Sundermeier, Thomas
Sakami, Sanae
Sahu, Bhubanananda
et al.

Publication Date

2017-02-24

DOI

10.1074/jbc.M116.770024

Peer reviewed

MicroRNA-processing Enzymes Are Essential for Survival and Function of Mature Retinal Pigmented Epithelial Cells in Mice[*]

Thomas R. Sundermeier[‡], **Sanae Sakami**[‡], **Bhubanananda Sahu**[§], **Scott J. Howell**[§], **Songqi Gao**[‡], **Zhiqian Dong**[¶],
Marcin Golczak[‡||], **Akiko Maeda**[§1], and **Krzysztof Palczewski**[‡||2]

From the Departments of ‡Pharmacology and §Ophthalmology and Visual Sciences, School of Medicine, and the ||Cleveland Center for Membrane and Structural Biology, Case Western Reserve University, Cleveland, Ohio 44106 and ¶Polgenix, Inc., Cleveland, Ohio 44106

Edited by Paul E. Fraser

Age-related macular degeneration (AMD) is a major cause of irreversible vision loss. The neovascular or "wet" form of AMD can be treated to varying degrees with anti-angiogenic drugs, but geographic atrophy (GA) is an advanced stage of the more prevalent "dry" form of AMD for which there is no effective treatment. Development of GA has been linked to loss of the microRNA (miRNA)-processing enzyme DICER1 in the mature retinal pigmented epithelium (RPE). This loss results in the accumulation of toxic transcripts of *Alu* transposable elements, which activate the NLRP3 inflammasome and additional downstream pathways that compromise the integrity and function of the RPE. However, it remains unclear whether the loss of miRNA processing and subsequent gene regulation in the RPE due to DICER1 deficiency also contributes to RPE cell death. To clarify the role of miRNAs in RPE cells, we used two different mature RPE cell-specific *Cre* recombinase drivers to inactivate either *Dicer1* or DiGeorge syndrome critical region 8 (*Dgcr8*), thus removing RPE miRNA regulatory activity in mice by disrupting two independent and essential steps of miRNA biogenesis. In contrast with prior studies, we found that the loss of each factor independently led to strikingly similar defects in the survival and function of the RPE and retina. These results suggest that the loss of miRNAs also contributes to RPE cell death and loss of visual function and could affect the pathology of dry AMD.

Age-related macular degeneration (AMD)[3] is a progressive retinal degenerative disorder that preferentially impacts the macula, the central region of the retina primarily responsible for both color vision and visual acuity. AMD is the leading cause of irreversible vision loss in modern Western societies among adults over 50 and is projected to impact the lives of nearly 200 million people worldwide by the year 2020 (1–4). It presents in two distinct forms, based on the types of lesions that occur in the late stages. The neovascular or "wet" form of AMD is associated with abnormal growth of blood vessels in the choriocapillaris, which extend through Bruch's membrane and cause acute vision loss that can be reversed relatively rapidly through intravitreal injection of vascular endothelial growth factor (VEGF) inhibitors (5–8). In contrast, the dry form of AMD is characterized by a large number of drusen and occasionally by geographic atrophy (GA), the regional loss of macular photoreceptors, retinal pigmented epithelium (RPE), and choriocapillaris. These changes cause deficits in dark adaptation, along with dense visual field scotomas and a gradual decline in visual acuity (9–11). Currently, there is no effective treatment for the dry form of AMD.

Discovered over 2 decades ago in *Caenorhabditis elegans*, miRNAs regulate gene expression at the post-transcriptional level (12, 13). miRNA biogenesis involves two sequential cleavage steps. The first is accomplished in the nucleus by the microprocessor complex and involves a member of the ribonuclease III superfamily of dsRNA-specific endoribonucleases, DROSHA, and its required cofactor DGCR8 (DiGeorge syndrome critical region 8). The second cleavage step is catalyzed in the cytoplasm by another ribonuclease III-type enzyme, DICER1. Through imperfect complementarity with target sites on messenger RNAs (mRNAs), miRNAs recruit the miRNA-induced silencing complex, which represses gene expression primarily by destabilizing mRNA, but also by reducing the rate of protein translation (14). In addition to their well characterized roles in cell and tissue development, miRNAs in post-mitotic cells often are critical in coping with cellular stress (15–

18). Within the eye, the physiology of photoreceptor cells presents a unique set of challenges, necessitating precise tuning of gene regulatory networks to maintain cell survival and function. Unsurprisingly, studies on the functional roles of miRNAs in retinal photoreceptors have firmly established that miRNAs are essential for the survival and function of these perpetually stressed post-mitotic cells (19–24). Conditional knock-out of the miRNA biogenesis factor *Dicer1* specifically in mature rods led to progressive retinal degeneration in mice (19). Similarly, the absence of *Dgcr8* in post-mitotic cone photoreceptors caused loss of their outer segments (OSs) and deterioration of light responses (20). In addition, loss of the post-mitotic photoreceptor enriched miR-183 cluster resulted in increased sensitivity to retinal degeneration during aging or after exposure to intense light (21, 22).

The RPE, a monolayer of cells lying adjacent to the photoreceptor outer segment layer, is another vulnerable, perpetually stressed intraocular cell type. RPE cells perform a myriad of functions, including absorbing stray photons of light, maintaining the pH and nutrient content of the subretinal space, participating in the regeneration of visual chromophore, and phagocytizing the outermost portion of photoreceptor outer segments. Roughly 10% of each photoreceptor cell in the human retina is phagocytosed on a daily basis, making RPE cells probably the most active phagocytic cells in the body (25) (reviewed in Refs. 26 and 27). This phagocytic process removes photooxidation products, including lipids and proteins from the photoreceptors, generated due to high levels of oxygen and light exposure and accumulated in the RPE. Thus, RPE cells are constantly subjected to toxic metabolic by-products. Finely tuned gene regulatory networks also could help to cope with this type of continuous cellular stress.

Inhibition of either of the two most abundantly expressed RPE miRNAs, miR-204 and -211, in human fetal RPE cells results in increased proliferation and decreased transepithelial monolayer electrical resistance as well as altered expression of tight junction genes (28, 29). However, inhibition of both miRNAs causes a more general loss of RPE-specific gene expression accompanied by morphological changes and increased expression of genes causing epithelial to mesenchymal transition (28). RPE cell-specific miRNA loss-of-function models in animals have clearly demonstrated that miRNAs are essential for proper specification and differentiation of RPE cells (24, 28, 30). However, available data addressing their roles in the physiology and function of mature RPE cells *in vivo* are limited.

Kaneko *et al.* (31) demonstrated that the miRNA biogenesis factor, DICER1, is down-regulated in the RPE of patients with GA. This result led to the intriguing possibility that loss of RPE miRNAs could be associated with the development or progression of GA. These mice evidenced abnormal RPE morphology and RPE cell death, a phenotype also observed upon injection of an adeno-associated virus (AAV) driving RPE-specific expression of *Cre* (tyrosine recombinase) in mice with conditional *Dicer1* cKO alleles. Surprisingly, injection of the same AAV into mice carrying conditional alleles for *Drosha*, *Dgcr8*, or miRNA binding enzyme Argonaute 2 (*Ago2*) failed to elicit similar defects in RPE survival (31). Normal RPE morphology was also
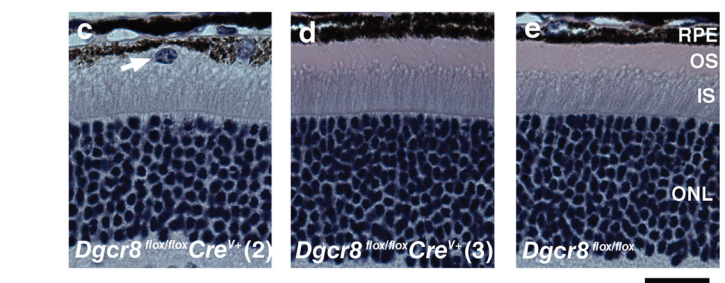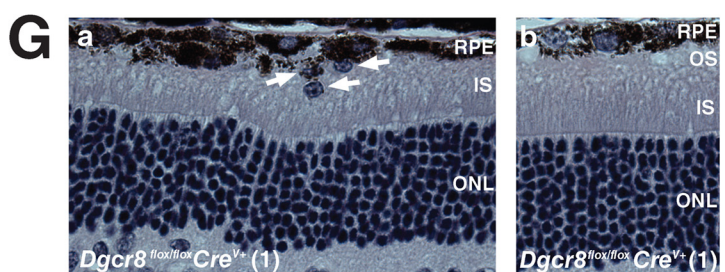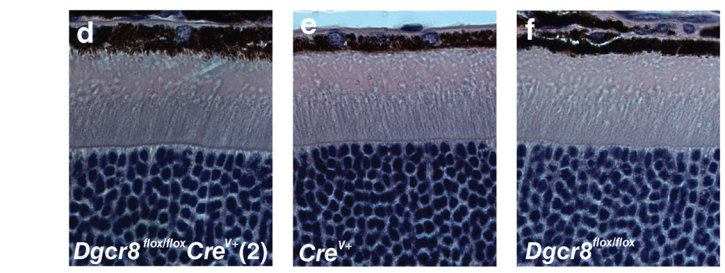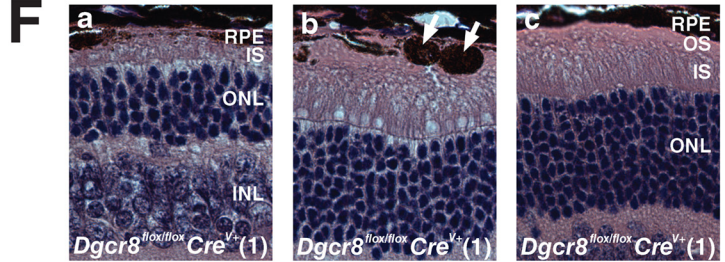
observed in *Ago1*, *Ago3*, and *Ago4* knock-out mice. This led to the conclusion that the RPE disruption associated with loss of DICER1 was miRNA-independent. RPE cell degeneration was instead attributed to failure of DICER1-mediated degradation of toxic transcripts of *Alu* transposable elements in humans and similar rodent short interspersed nuclear elements (SINE), B1 and B2, in mice. Indeed, exogenous introduction of *Alu* element-encoded RNAs has been shown to induce RPE abnormalities (32–37), but it remains unclear whether loss of miRNAs also plays a role in RPE cell death in the absence of DICER1.

Thus, to clarify the contribution of miRNA loss to the molecular mechanism underlying the pathology of DICER1 absence in the mature RPE, we performed a systematic characterization of RPE-specific conditional knockouts of *Dicer1* and *Dgcr8* in mice using two independent *Cre* lines. In contrast to studies involving viral delivery of *Cre*, we found that loss of DGCR8 or DICER1 in mature RPE cells resulted in strikingly similar defects in the morphology and function of the RPE. These results strongly suggest that miRNAs are important for the survival and function of these vulnerable post-mitotic cells and that miRNA loss could contribute to the mechanism of RPE cell death in GA.

Results

Mature RPE-specific Dicer1 and Dgcr8 cKO Mice Exhibited Similar Patterns of RPE and Retinal Degeneration—We generated mature RPE cell-specific *Dgcr8* and *Dicer1* cKO mice by breeding *Dgcr8^{flox/flox}* (38) or *Dicer1^{flox/flox}* (39) mice with a *Cre* mouse line exhibiting doxycycline-inducible expression of *Cre* recombinase s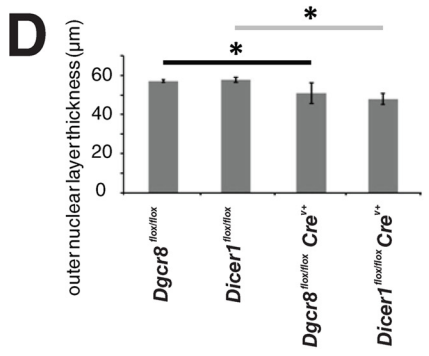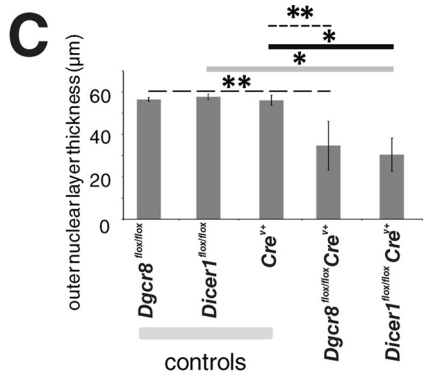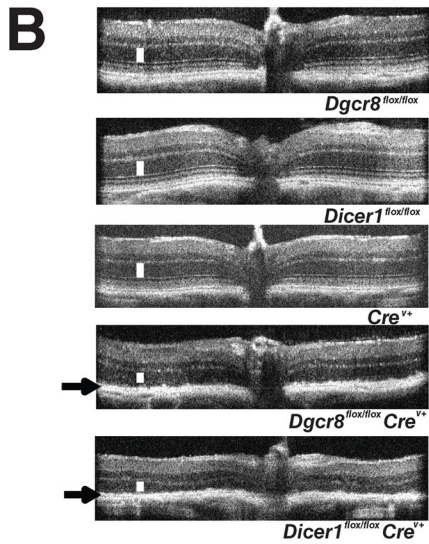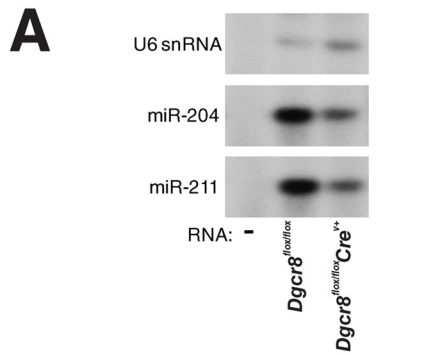pecifically in mature RPE cells driven by a fragment of the human vitelliform macular dystrophy-2 (VMD2) promoter (P(VMD2))-directed reverse tetracycline-dependent transactivator (rtTA) and the tetracycline-responsive element (TRE)-directed Cre^{v+} (pVMAD2-rtTA-TRE-*Cre*) (40) and a 2.9-kb non-inducible human Ca^{2+}-activated anion channel Bestrophin 1 (*Best1*) gene promoter (41). *Best1* is highly expressed in the RPE (42).

Splinted ligation demonstrated that levels of the RPE cell-enriched miRNAs miR-204 and -211 were dramatically reduced in 5-week-old *Dgcr8^{flox/flox}*pVMAD2-rtTA-TRE-*Cre*^+ (*Dgcr8^{flox/flox}Cre^{v+}*) animals as compared with control Cre^{v+} littermates lacking *Cre* recombinase expression (Fig. 1*A*). We then performed *in vivo* spectral domain optical coherence tomography (SD-OCT) to determine the impact of loss of either *Dicer1* or *Dgcr8* on the intraocular morphology of 8-week-old animals. (A more comprehensive interpretation of OCT images can be found elsewhere (43, 44)). For both *Dicer1^{flox/flox}Cre^{v+}* and *Dgcr8^{flox/flox}Cre^{v+}* animals, we observed abnormal reflectivity in the region corresponding to the RPE along with a decrease in the thickness of the outer nuclear layer (ONL), where nuclei of rod and cone photoreceptors are found (Fig. 1, *B* and *C*). Consistent with the reported mosaic distribution of Cre^{v+} expression in the parental mouse line (40), the extent of outer nuclear layer thinning was somewhat variable, both regionally within the same eye and from animal to animal (Fig. 1, *C* and *E–G*). In younger mice, the morphology of five animals per group was compared by different techniques in 5-week-old cKO animals and control litter-

mates. SD-OCT revealed similar, but less dramatic, outer nuclear layer thinning in both $Dicer1^{flox/flox}Cre^{v+}$ and $Dgcr8^{flox/flox}Cre^{v+}$ mice as compared with control animals (Fig. 1, *C*, *D*, and *G*). Hematoxylin and eosin (H&E) staining of sections of fixed paraffin-embedded eyes confirmed the reduction in length of photoreceptor OSs and revealed localized pigment deposits in 8-week-old $Dgcr8^{flox/flox}Cre^{v+}$ mice (Fig. 1, *E* and *F*). Moreover, a reduction in the ONL and disruption of the integrity of the RPE monolayer were observed in 8-week-old $Dicer1^{flox/flox}Cre^{v+}$ mice as compared with either control littermates lacking the *Cre* transgene or *Cre*-expressing control animals with wild-type alleles of *Dicer1* and *Dgcr8* (Fig. 1, *E* and *F*). In addition, immunostaining for the tight junction protein zonula occludens 1 (ZO-1) in flat mounts of RPE (RFM) showed a loss of monolayer organization in $Dgcr8^{flox/flox}Cre^{v+}$ mice relative to control $Dgcr8^{flox/flox}$ or Cre^{v+} animals (Fig. 2*A*).
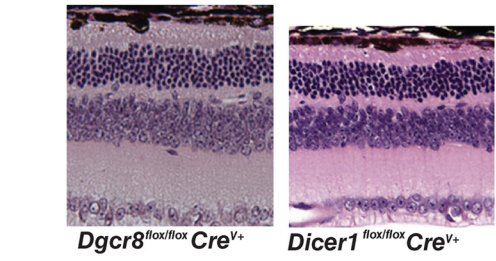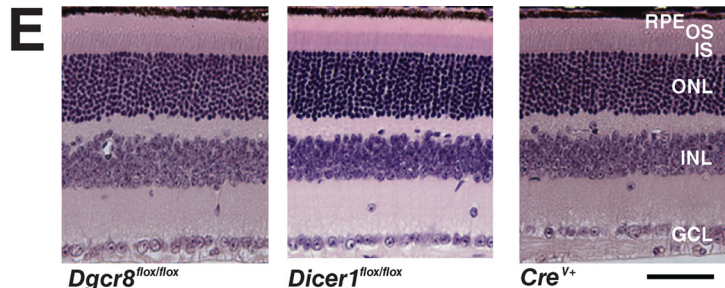
In younger, 5-week-old mice, H&E staining of fixed tissue sections also revealed that varying degrees of shortening of OSs had occurred regionally within the same eye and from animal to animal (Fig. 1*G*). Indeed, only about three of five 5-week-old animals exhibited morphological defects, seen as shortening of OSs or the migration of cells into the interphotoreceptor space (Fig. 1, *G* (*a–c*)). Two of five $Dgcr8^{flox/flox}Cre^{v+}$ mice evidenced morphologically normal photoreceptors and RPE (Fig. 1, *G* (*d*)) identical to those of $Dgcr8^{flox/flox}$ control mice (Fig. 1*G* (*e*)). Regions of loss in RPE layer integrity were also less frequent and pronounced at this age. $Dicer1^{flox/flox}Cre^{v+}$ and $Dgcr8^{flox/flox}Cre^{v+}$ animals were similar as to their extent of retinal degeneration, suggesting a similar time course for the development of morphological changes. Altogether, comparing 5- and 8-week-old animals revealed the progressive character of this process.

Loss of Dgcr8 in the Mature RPE Leads to Defects in Retina and RPE Function—To assess the impact of *Dicer1* or *Dgcr8* cKO on visual function, we performed electroretinogram (ERG) recordings on 8-week-old cKO and control mice. Consistent with the observed changes in morphology, ERGs revealed defects in both rod and cone photoreceptor visual responses that were of similar magnitudes in $Dicer1^{flox/flox}Cre^{v+}$ and $Dgcr8^{flox/flox}Cre^{v+}$ mice (Fig. 2*B*). Next, we compared the efficiency of RPE phagocytosis of photoreceptor outer segment discs between $Dgcr8^{flox/flox}Cre^{v+}$ mice and

control animals by measuring the number of rhodopsin-containing structures present in the RPE after immunostaining. Here we found a reduction in opsin-stained foci in the RPE of $Dgcr8^{flox/flox}Cre^{v+}$ mice relative to controls near the morning circadian peak of phagocytosis activity (Fig. 3, *A* and *B*). Finally, we measured the rate of recovery of the visual chromophore, 11-*cis*-retinal, after photobleaching 5-week-old $Dgcr8^{flox/flox}Cre^{v+}$ mice and control animals to determine whether visual cycle activity was impaired in the absence of *Dgcr8*. $Dgcr8^{flox/flox}Cre^{v+}$ mice showed a significant reduction in chromophore levels at all time points measured (Fig. 3*C*).

Phagosomes and Lipid Droplet-like Structures Accumulate in the RPE of the $Dgcr8^{flox/flox}Cre^{v+}$ Mouse—To further analyze the initial impact of Dgcr8 loss in mature RPE, we analyzed the ultrastructure of the RPE and OS in 5-week-old $Dgcr8^{flox/flox}Cre^{v+}$ and $Dgcr8^{flox/flox}$ control mice (Fig. 4*A*, *a–f*). One of four $Dgcr8^{flox/flox}Cre^{v+}$ mice showed various degrees of RPE defects and OS shortening (Fig. 4*A*, *a*). RPE cells adjacent to shortened OSs contained unusually high numbers of phagosomes and lipid droplet-like structures. Notably, the phagosomes contained OSs (Fig. 4*A* (*a*), *arrowheads*), and their high magnification images revealed remnant disc membrane structures inside (Fig. 4, *B* (*b*) and *C* (*d*)). Lipid droplet-like structures contained electron-dense homogeneous material with a more electron-dense ring at the rim (Fig. 4*A* (*a*), *asterisks*). High magnification images of lipid droplet-like structures did not reveal membranous material inside (Fig. 4, *B* (*a*), *C* (*a*), and *C* (*b*)). Phagosomes were also noted in the RPE of a $Dgcr8^{flox/flox}$ control mouse, but their number was significantly lower than that observed in the affected RPE from a $Dgcr8^{flox/flox}Cre^{v+}$ mouse. Lipid droplet-like structures were morphologically closed to lipid inclusion droplets reported by Robison and Kuwabara (45). However, lipid droplets evidenced by transmission electron microscopy (TEM) revealed a homogeneous electron opacity containing a slightly lighter cortical zone (45). In contrast, lipid droplet-like structures that we observed in $Dgcr8^{flox/flox}Cre^{v+}$ mice featured electron-dense rings at their rims. Higher magnification TEM analyses of rim regions from lipid droplet-like structures showed a single electron-dense layer (Fig. 4, *C* (*a*) and *C* (*b*), *arrowheads*). In contrast, mitochondrial outer membranes (Fig. 4, *C* (*a*) and *C* (*b*), *arrows*) and phagosomal membranes (Fig. 4, *C* (*c*) and *D* (*d*), *arrows*) con-

FIGURE 1. **Mature RPE-specific *Dgcr8^{flox/flox}Cre^{v+}* and *Dicer1^{flox/flox}Cre^{v+}* mice exhibit retinal degeneration.** *A*, splinted ligation revealed a reduction in the levels of RPE-enriched miR-204 and -211 in 5-week-old inducible $Dgcr8^{flox/flox}Cre^{v+}$ mice as compared with control littermates. U6 snRNA was used as a loading control. *B*, SD-OCT showed a reduction in outer nuclear layer thickness (*white line*) and abnormalities in the RPE/retina interface (*black arrows*) where pigmented granules occasionally were deposited in 8-week-old $Dgcr8^{flox/flox}Cre^{v+}$ and $Dicer1^{flox/flox}Cre^{v+}$ mice. *C*, quantification of outer nuclear layer thickness from OCT measurements in 8-week-old inducible $Dgcr8^{flox/flox}Cre^{v+}$ mice. *Error bars*, S.D. Measurements were made from at least 5 mice/genotype. *, $p < 0.05$; **, $p < 0.001$. *D*, quantification of outer nuclear layer thickness in 5-week-old $Dicer1^{flox/flox}Cre^{v+}$ and $Dgcr8^{flox/flox}Cre^{v+}$ mice. *Error bars*, S.D. of measurements obtained from 5 animals/genotype. *, $P < 0.05$. *E*, outer nuclear layer thinning and disruption of the RPE monolayer were observed in H&E-stained sections of paraffin-embedded fixed eyes from 8-week-old $Dicer1^{flox/flox}Cre^{v+}$ and $Dgcr8^{flox/flox}Cre^{v+}$ mice. *Scale bar*, 40 µm. *F*, higher magnification images of 8-week-old $Dgcr8^{flox/flox}Cre^{v+}$ and control mouse eyes show various degrees of photoreceptor cell degeneration in five of six $Dgcr8^{flox/flox}Cre^{v+}$ mice. In severely affected regions, OSs had completely degenerated, and inner segment (*IS*) and ONLs were dramatically thinner (*a*). Pigment granules were occasionally deposited where photoreceptor cells had degenerated (*arrows* in *b*). Less affected regions of the same retina were characterized by shortened OSs without any pigment granule deposits (*c*). One of the six $Dgcr8^{flox/flox}Cre^{v+}$ mice had no evidence of photoreceptor cell degeneration (*d*). Cre^{v+} control (*e*) and $Dgcr8^{flox/flox}$ control (*f*) mice did not exhibit photoreceptor cell degeneration. Images of two different $Dgcr8^{flox/flox}Cre^{v+}$ mice are labeled as $Dgcr8^{flox/flox}Cre^{v+}$ (*1*) and $Dgcr8^{flox/flox}Cre^{v+}$ (*2*). *Scale bar*, 20 µm. *INL*, inner nuclear layer; *GCL*, ganglion cell layer. *G*, higher magnification images of paraffin sections from 5-week-old $Dgcr8^{flox/flox}Cre^{v+}$ mice and control littermates show variable phenotypic outcomes for individual animals and different retinal regions of the same animal. Three of five $Dgcr8^{flox/flox}Cre^{v+}$ mice showed short OSs and cells that migrated to the interphotoreceptor space. Such cells were observed only occasionally (*arrows* in *a* and *c*). Variability of phenotypic outcome was also noted for different regions of the same retinal section (*e.g.* nearly completely degenerated OSs and migrated cells (*arrows* in *a*) or shortened OSs (*b*)). Two of five $Dgcr8^{flox/flox}Cre^{v+}$ mice did not show photoreceptor degeneration (*d*); nor did $Dgcr8^{flox/flox}$ control mice evidence photoreceptor degeneration (*e*). Images of three different $Dgcr8^{flox/flox}Cre^{v+}$ mice are labeled as $Dgcr8^{flox/flox}Cre^{v+}$ (*1*), $Dgcr8^{flox/flox}Cre^{v+}$ (*2*), and $Dgcr8^{flox/flox}Cre^{v+}$ (*3*). *Scale bar*, 20 µm.
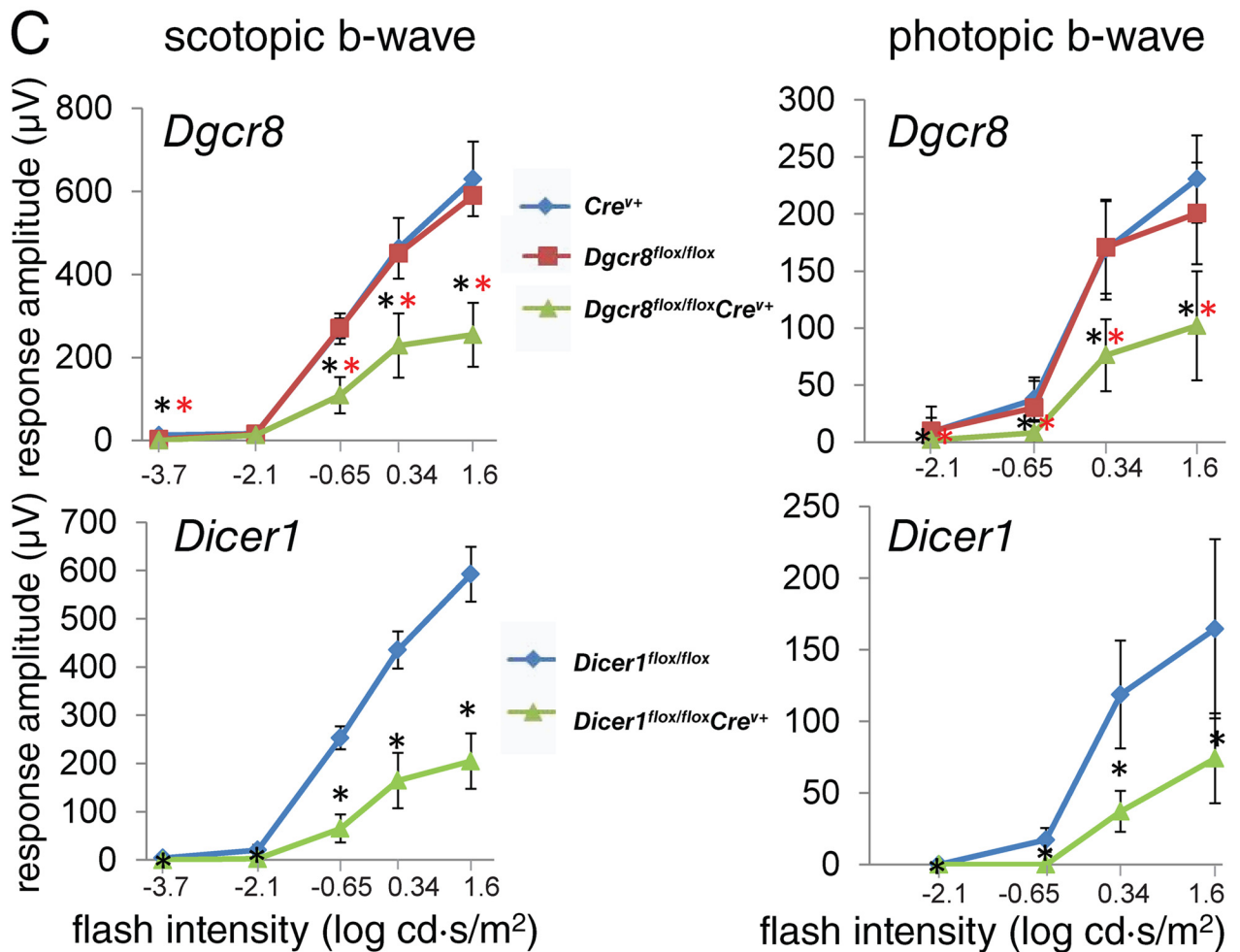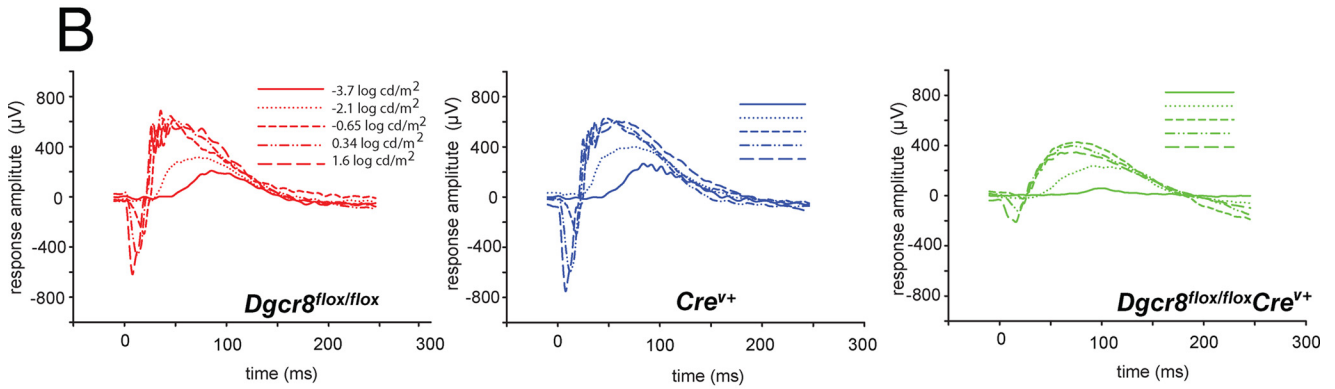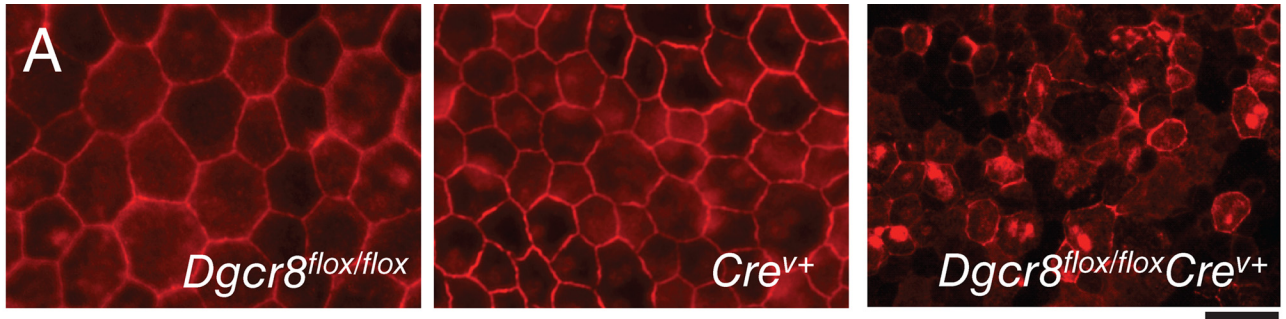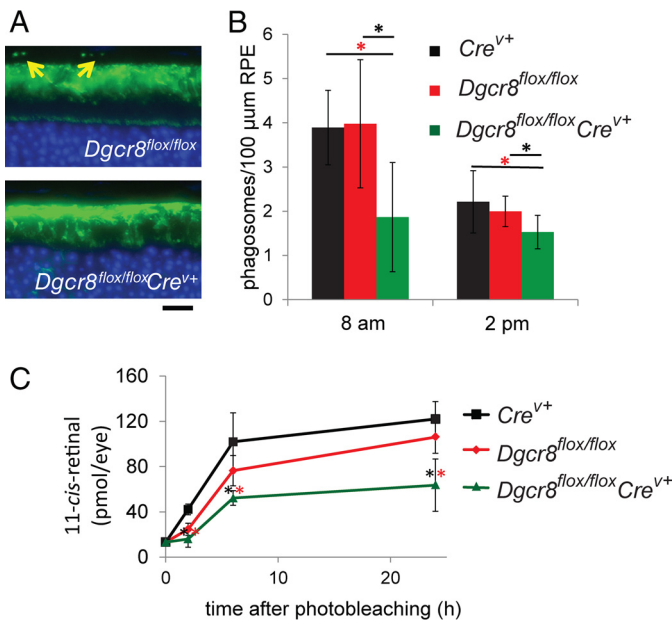
FIGURE 3. **Inducible mature RPE-specific *Dgcr8^flox/flox^Cre^v+^* mice are defective in phagocytosis of photoreceptor outer segment discs and regeneration of visual chromophore.** *A*, immunostaining with an anti-opsin antibody shows foci in the RPE layer (indicated by *yellow arrows*) that correspond to phagocytosed rod outer segment discs in 8-week-old mice. *Scale bar*, 25 μm. *B*, quantitation of the number of phagosomes in *Dgcr8^flox/flox^Cre^v+^* animals near the morning peak and afternoon trough of circadian regulated RPE phagocytosis revealed a reduction in the quantity of opsin-containing foci in the RPE of 8-week-old *Dgcr8^flox/flox^Cre^v+^* mice compared with control animals. *p* values were <0.001 calculated for *Dgcr8^flox/flox^Cre^v+^* versus *Dgcr8^flox/flox^* (*black asterisks*) and *Dgcr8^flox/flox^Cre^v+^* versus *Cre^v+^* (*red asterisks*). *C*, analysis of the rate of recovery of the visual chromophore 11-*cis*-retinal after illumination in 5-week-old *Dgcr8^flox/flox^Cre^v+^* mice and control animals revealed reduced chromophore levels in cKO animals at all studied time points. *Error bars*, S.D. based on quantification of at least 5 animals/genotype at each time point.

sisted of phospholipid bilayers and were observed as double layers. These data suggest that the rim of a lipid-droplet-like structure is composed of a phospholipid monolayer. Reportedly, the surface of a lipid droplet also consists of a phospholipid monolayer (46). Thus, the lipid droplet-like structures that we observed could actually be lipid droplets with their electron-dense rings inside representing unique lipid components. Such structures were occasionally seen in two of three of the *Dgcr8^flox/flox^Cre^v+^* mice without shortening of their OSs. Also, in one *Dgcr8^flox/flox^Cre^v+^* mouse with various degrees of RPE defects and shortening of the OSs, an RPE cell adjacent to normal OSs occasionally featured a lipid droplet-like structure (Fig. 4, *A* (*b*), *asterisk*). We did not see a lipid droplet-like structure in one *Dgcr8^flox/flox^* control mouse. Together these data suggest that the lack of Dgcr8 in mature RPE causes either a defect in digesting phagocytosed material or excessive phagocytosis *per se*. Also, lack of Dgcr8 in mature RPE could potentially cause defects in lipid metabolism. The same data also imply

that lack of Dgcr8 in the mature RPE causes shortening of adjacent OSs.

Mature RPE-specific Dgcr8 cKO Driven by a Non-inducible Cre Expression Cassette Results in a Similar Pattern of Retinal Degeneration and Functional Impairment—To confirm that the morphological and functional defects observed in mature RPE cell-specific *Dgcr8^flox/flox^Cre^v+^* mice did not depend on the mouse strain or specific *Cre* driver used to elicit gene excision, we generated independent *Dicer1* and *Dgcr8* cKO mouse lines by crossing *Dicer1^flox/flox^* or *Dgcr8^flox/flox^* mice with a different mature RPE cell-specific *Cre*-expressing line driven by a smaller fragment of the *Best1* gene promoter with *Cre* expression independent of doxycycline administration (*Dicer1^flox/flox^Cre^B+^* and *Dgcr8^flox/flox^Cre^B+^*) (41). Surprisingly, these mice evidenced a mottled pattern of black and white fur (Fig. 5*A*). The presence of white fur was specific to the cKO animals because white fur was absent from both littermates lacking *Cre* expression and control mice derived from the parental *Cre^B+^*-expressing line. However, both *Dicer1^flox/flox^Cre^B+^* and *Dgcr8^flox/flox^Cre^B+^* mice exhibited this mottled coat color phenotype, although its severity varied from animal to animal, suggesting different expression levels of *Cre*, as shown in Fig. 5*B*. Although *Cre* recombinase expression for both lines used in this study was restricted to mature RPE cells within the eye (41), the *Best1* gene is also reportedly expressed in melanocytes. Thus, it is possible that loss of miRNAs in melanocytes could cause pigmentary changes resulting in alterations in coat color. Indeed, several melanocyte miRNAs are linked to either melanocyte survival or pigmentation processes (47–51). Therefore, we hypothesized that the link between coat color and the severity of retinal degeneration might arise from *Cre* expression patterns that vary from animal to animal but remain consistent within the pigmentary cells of the same animal.

Therefore, we divided the cKO animals from each line into three groups (*i.e.* those with entirely black fur, those whose fur was roughly 5–10% white, and those with fur roughly 40–60% white); mice from each group were present in roughly equal proportions in the total population. We then employed SD-OCT to determine whether 8-week-old *Dicer1^flox/flox^Cre^B+^* and/or *Dgcr8^flox/flox^Cre^B+^* mice displayed differences in intraocular morphology consistent with the cKO mice described previously. Not surprisingly, OCT revealed evidence of retinal degeneration in a subset of both *Dicer1^flox/flox^Cre^B+^* and *Dgcr8^flox/flox^Cre^B+^* mice. However, we were surprised to find that the pattern of retinal degeneration was proportional to the presence of white fur in both *Dicer1^flox/flox^Cre^B+^* and *Dgcr8^flox/flox^Cre^B+^* mice, with mice in the group exhibiting ~40–60% white fur showing significantly more severe thinning of the ONL (Fig. 6, *A* and *B*). Next, we performed quanti-

FIGURE 2. **RPE integrity and visual function are impaired in both inducible *Dgcr8^flox/flox^Cre^v+^* and *Dicer1^flox/flox^Cre^v+^* mice.** *A*, immunostaining of flat mounted RPE for the tight junction protein ZO-1 revealed a disruption of RPE organization in 8-week-old *Dgcr8^flox/flox^Cre^v+^* mice. *Scale bar*, 50 μm. *B*, single-flash ERG responses of increasing light intensity for and *Dgcr8^flox/flox^*, *Cre^v+^*, and *Dgcr8^flox/flox^Cre^v+^* mice were obtained under dark-adapted conditions. *C*, ERG recordings revealed a reduction in both scotopic *a*-wave and photopic *b*-wave amplitudes, reflective of rod- and cone-driven vision, respectively, in 8-week-old *Dgcr8^flox/flox^Cre^v+^* and *Dicer1^flox/flox^Cre^v+^* mice as compared with control animals. *Error bars*, S.D. from measurements of at least 5 animals/genotype and time point. *p* values were <0.001 calculated for *Dgcr8^flox/flox^Cre^v+^* versus *Dgcr8^flox/flox^* or *Dicer1^flox/flox^Cre^v+^* versus *Dicer1^flox/flox^* (*black asterisks*) and *Dgcr8^flox/flox^Cre^v+^* versus *Cre^v+^* (*red asterisks*)
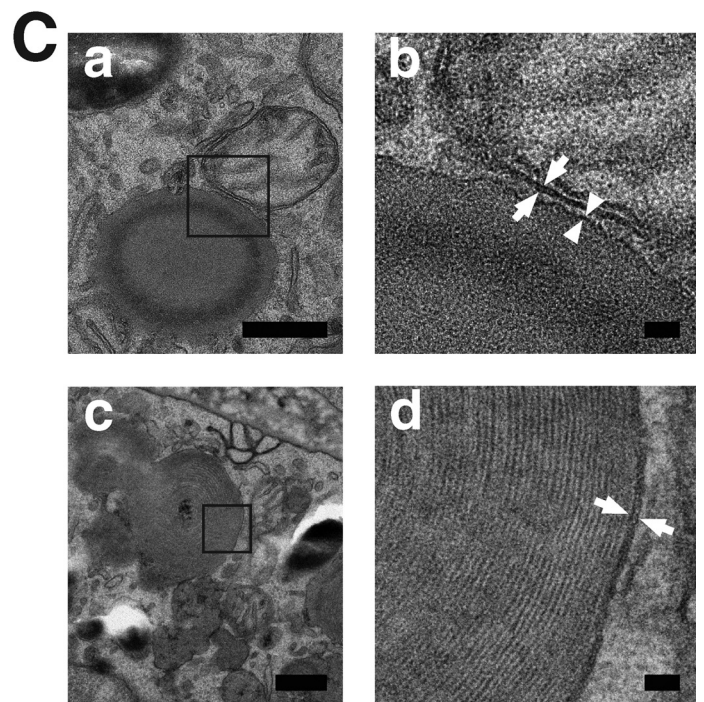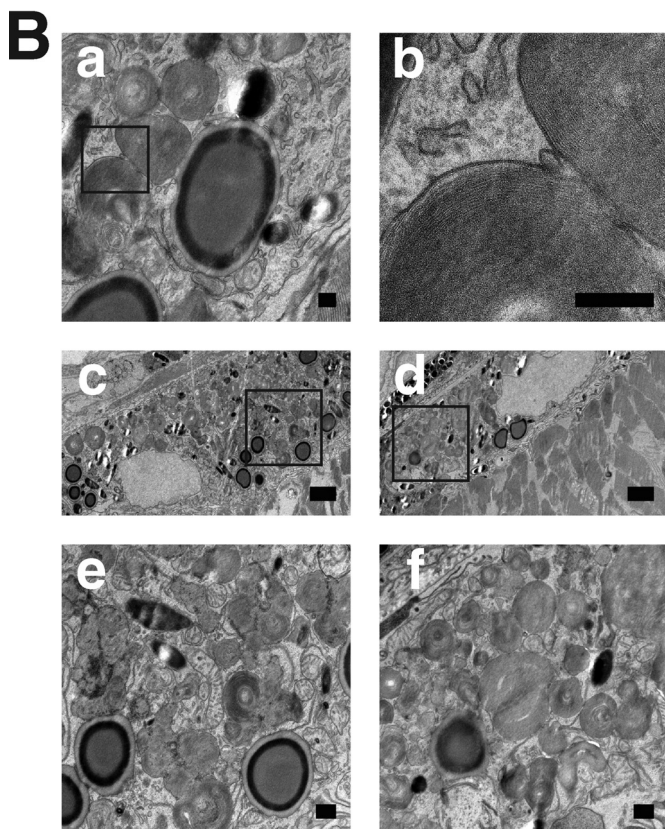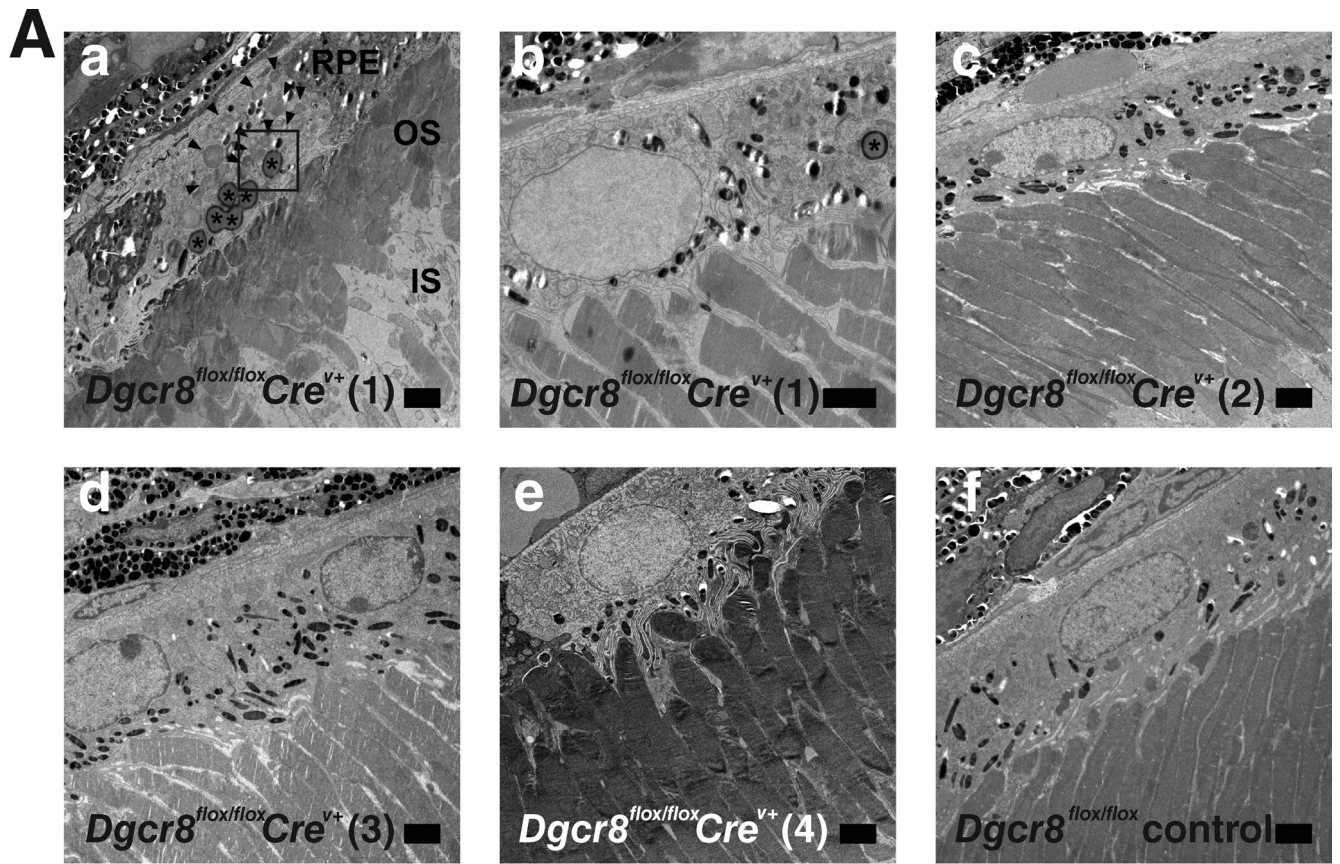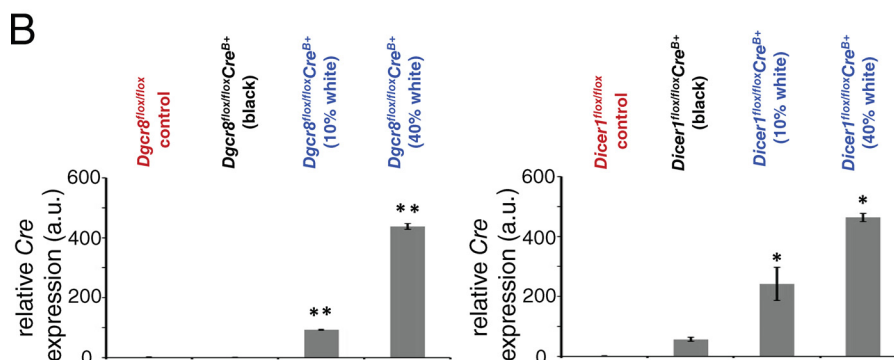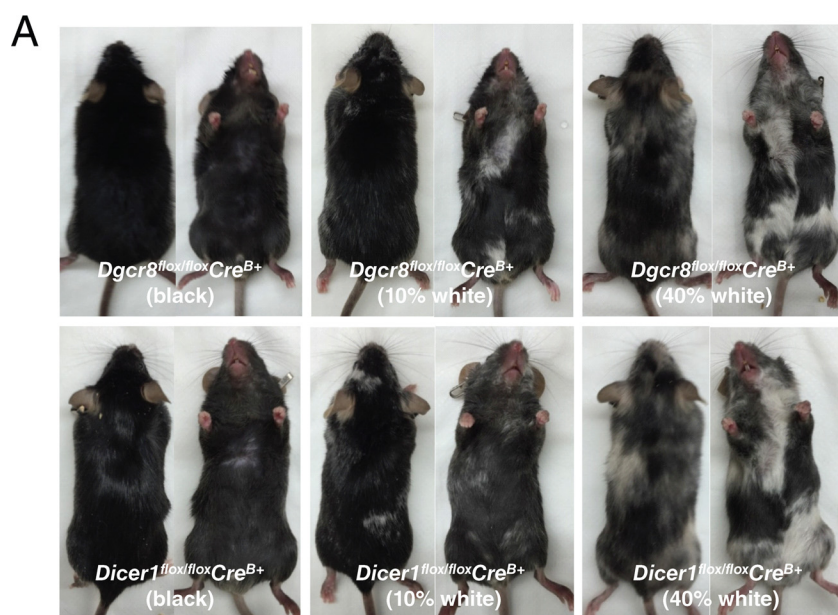
FIGURE 5. Coat color correlates with Cre expression in the RPE of constitutive *Dicer1^flox/flox^Cre^B+^* and *Dgcr8^flox/flox^Cre^B+^* mice. *A*, images of mature RPE-specific *Dicer1^flox/flox^Cre^B+^* and *Dgcr8^flox/flox^Cre^B+^* mice reveal variations in coat color. *B*, quantitative RT-PCR analysis of *Cre* recombinase gene expression in the RPE/choroid of 8-week-old *Dicer1^flox/flox^Cre^B+^* and *Dgcr8^flox/flox^Cre^B+^* mice with different proportions of white and black fur, along with control littermates revealed that mice with more white fur also exhibited higher *Cre* expression in the RPE/choroid. *, $p < 0.05$; **, $p < 0.001$.

tative real time-PCR (RT-PCR) analyses on total RNA derived from the RPE/choroid compartment of control *Dicer1^flox/flox^* and *Dgcr8^flox/flox^* mice and cKO mice exhibiting either no white fur, 5–10% white fur, or 40–60% white fur. We found that *Cre* expression in the back of the eye correlated with the amount of white fur (Fig. 5*B*). Histological analysis of 8-week-old *Dicer1^flox/flox^Cre^B+^* and *Dgcr8^flox/flox^Cre^B+^* mice with similar fractions of white fur confirmed the defects in RPE morphology

and the number of photoreceptor nuclei (Fig. 6*C*) but varied in severity. Similarly, ZO-1 staining of RFM revealed defects in RPE monolayer organization that were more severe in animals with more white fur (Fig. 7*A*). As with the previously described cKO mouse lines, visual function correlated with these morphological changes. The amplitudes of both rod and cone-driven visual responses were reduced in cKO animals, especially those displaying significant white fur, and similar defects

FIGURE 4. Shortening of OS and accumulation of phagosomes and lipid droplet-like structures in the RPE of *Dgcr8^flox/flox^Cre^v+^* mice. TEM retinal images from 5-week-old *Dgcr8^flox/flox^Cre^v+^* and *Dgcr8^flox/flox^* control mice are shown. TEM images of four *Dgcr8^flox/flox^Cre^v+^* mice (*Dgcr8^flox/flox^Cre^v+^* (*1*), *Dgcr8^flox/flox^Cre^v+^* (*2*), *Dgcr8^flox/flox^Cre^v+^* (*3*), and *Dgcr8^flox/flox^Cre^v+^* (*4*)) and one *Dgcr8^flox/flox^* control mouse are shown. *A*, variability of phenotypic outcome was noted for different regions of the same retinal sections from one *Dgcr8^flox/flox^Cre^v+^* mouse (*Dgcr8^flox/flox^Cre^v+^* (*1*)): shortened OSs and accumulation of phagosomes and lipid droplet-like structures in adjacent RPE (*asterisks* in *A* (*a*)) or normal OSs and RPE (*A* (*b*)). Phagosomes containing OSs are indicated by *arrowheads* in *A* (*a*). Lipid droplet-like structures designated by *asterisks* in *A* (*a* and *b*) contained homogeneous electron-dense material without any membrane structures and featured a more electron-dense ring at the rim. Plastic sections prepared from three of four *Dgcr8^flox/flox^Cre^v+^* mice (*Dgcr8^flox/flox^Cre^v+^* (*2*) to (*4*)) showed normal OSs and RPE (*A* (*c–e*)). Plastic sections prepared from *Dgcr8^flox/flox^* control mice also revealed normal OSs and RPE (*A* (*c–f*)). *B*, higher magnification images of phagosomes and lipid droplet-like structures in a *Dgcr8^flox/flox^Cre^v+^* (*1*) mouse indicated by the *box* in *A* (*a*) are shown in *B* (*a*) and with even more enhancement in *B* (*b*). Remnant disc membrane structures are evident. *B* (*c–f*), other examples of accumulated phagosomes and lipid droplet-like structures from *Dgcr8^flox/flox^Cre^v+^* mice (*1*). Higher magnification images of phagosomes and lipid droplet-like structures indicated by *boxes* in *B*, *c* and *d*, are shown in *B*, *e* and *f*, respectively. *C*, higher magnification images of lipid droplet-like structures and phagosomes from *Dgcr8^flox/flox^Cre^v+^* mice (*1*). *C* (*a*), a lipid droplet-like structure and a mitochondrion in the RPE. Higher magnification images of the rim region of lipid droplet-like structure indicated by a *box* in *C* (*a*) are shown in *C* (*b*). The rim of lipid droplet-like structure evidenced a single layer (*arrow*). In contrast, outer membrane of mitochondria showed double layers (*arrow*). *C* (*c*), Phagosomes in the RPE. Higher magnification images of the phagosome membrane indicated by the *box* in *C* (*c*) are shown in *C* (*d*). The phagosome membrane showed double layers (*arrow*). *IS*, inner segment. *Scale bars*, 2 μm (*A* and *B* (*c*) and *B* (*d*)), 200 nm (*B* (*a* and *b*)), 400 nm (*B* (*e* and *f*) and (*C* (*a* and *c*)), and 40 nm (*C* (*b* and *d*)).
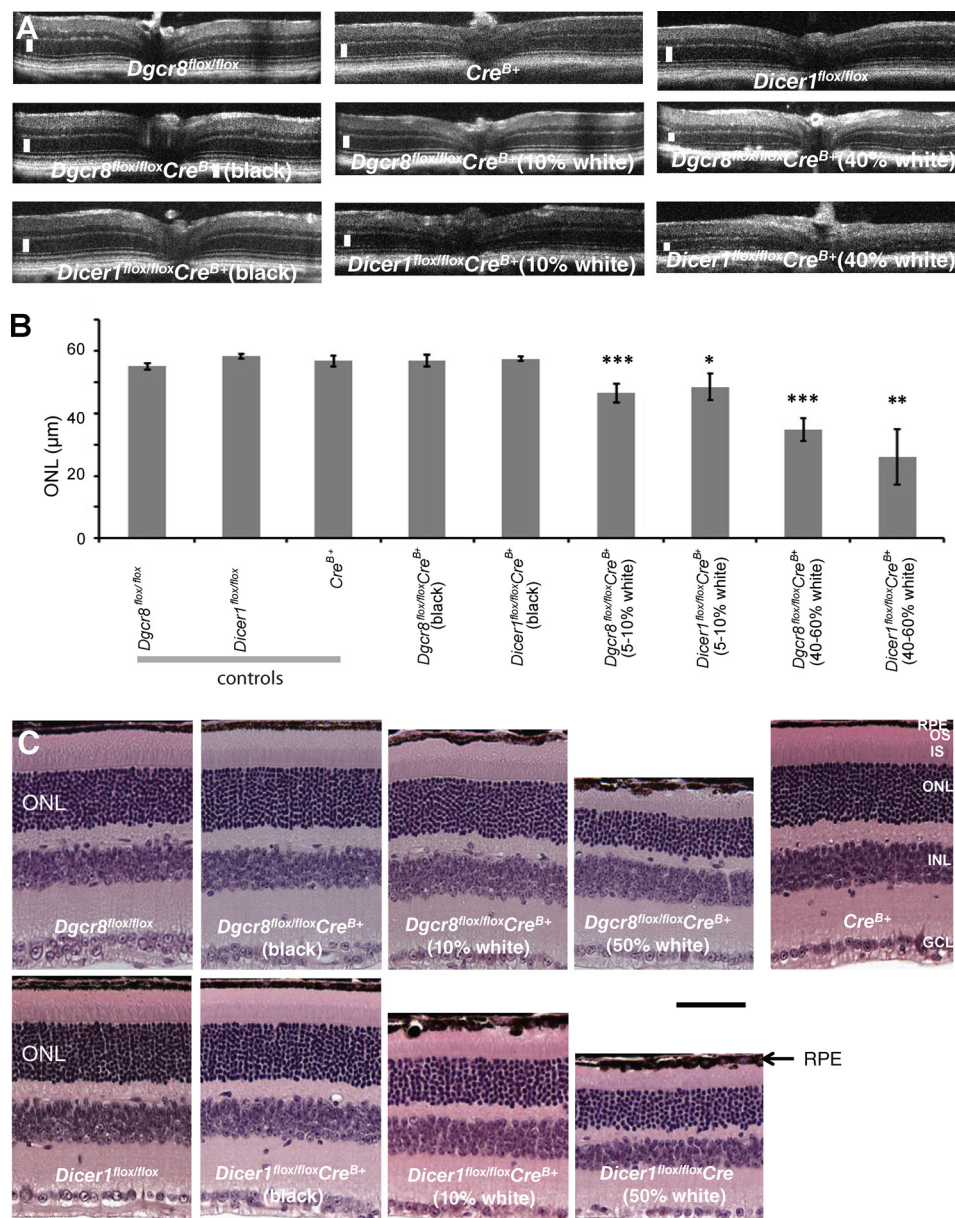
FIGURE 6. **The extent of retinal degeneration is proportional to the amount of white fur in mature RPE cell-specific *Dicer1^flox/flox^Cre^B+^* and *Dgcr8^flox/flox^Cre^B+^* mice.** *A*, SD-OCT revealed retinal degeneration in 8-week-old *Dicer1^flox/flox^Cre^B+^* and *Dgcr8^flox/flox^Cre^B+^* mice, especially in those mice with a high proportion of white fur. *White bars*, ONL layer. *B*, quantification of outer nuclear layer thickness demonstrates that photoreceptor cell degeneration occurred in both *Dicer1^flox/flox^Cre^B+^* and *Dgcr8^flox/flox^Cre^B+^* mice but was more pronounced in animals with more white fur. *C*, light microscopy of H&E-stained ocular tissue sections revealed loss of RPE monolayer integrity and reduction in ONL thickness in 8-week-old *Dicer1^flox/flox^Cre^B+^* and *Dgcr8^flox/flox^Cre^B+^* mice, especially in animals with a higher proportion of white fur. *Scale bar*, 40 μm. *p* values were statistically insignificant when calculated for *Dicer1^flox/flox^Cre^B+^* (black) *versus Dicer1^flox/flox^*, *Dicer1^flox/flox^Cre^B+^* (black) *versus Cre^B+^*, *Dicer1^flox/flox^Cre^B+^* (5–10%) *versus Cre^B+^*, *Dgcr8^flox/flox^Cre^B+^* (black) *versus Dgcr8^flox/flox^*, and *Dgcr8^flox/flox^Cre^B+^ versus Cre^B+^*; *, $p < 0.05$ for *Dicer1^flox/flox^Cre^B+^* (5–10%) *versus Dicer1^flox/flox^*, *Dicer1^flox/flox^Cre^B+^* (40–60%) *versus Dicer1^flox/flox^*, *Dgcr8^flox/flox^Cre^B+^* (5–10%) *versus Dgcr8^flox/flox^*, and *Dgcr8^flox/flox^Cre^B+^* (40–60%) *versus Dgcr8^flox/flox^*; *, $p < 0.001$ for *Dicer1^flox/flox^Cre^B+^* (40–60%) *versus Cre^B+^*, *Dgcr8^flox/flox^Cre^B+^ versus Cre^B+^*, and *Dgcr8^flox/flox^Cre^B+^ versus Cre^B+^*.

were noted in *Dicer1^flox/flox^Cre^B+^* and *Dgcr8^flox/flox^Cre^B+^* mice (Fig. 7B).

Discussion

The results presented here demonstrate that loss of DGCR8, a component of the nuclear microprocessor complex needed to support the first cleavage step of miRNA biogenesis, is essential for the survival and function of mature post-mitotic RPE cells in mice. Using two independent RPE cell-specific *Cre* recombinase-expressing mouse lines, we found a remarkable similarity

in the phenotypic consequences of Dgcr8 loss and Dicer1 loss. Dicer1 is the enzyme responsible for the second, cytoplasmic cleavage step associated with processing of mature miRNAs. These results strongly suggest that along with accumulation of *Alu* element-derived RNAs (31), loss of miRNAs plays a fundamental role in the mechanism of RPE cell death in the absence of DICER1.

A previous report showed that AAV-mediated delivery of a *Cre* recombinase expression cassette to the RPE of mice carrying conditional alleles for the microprocessor components
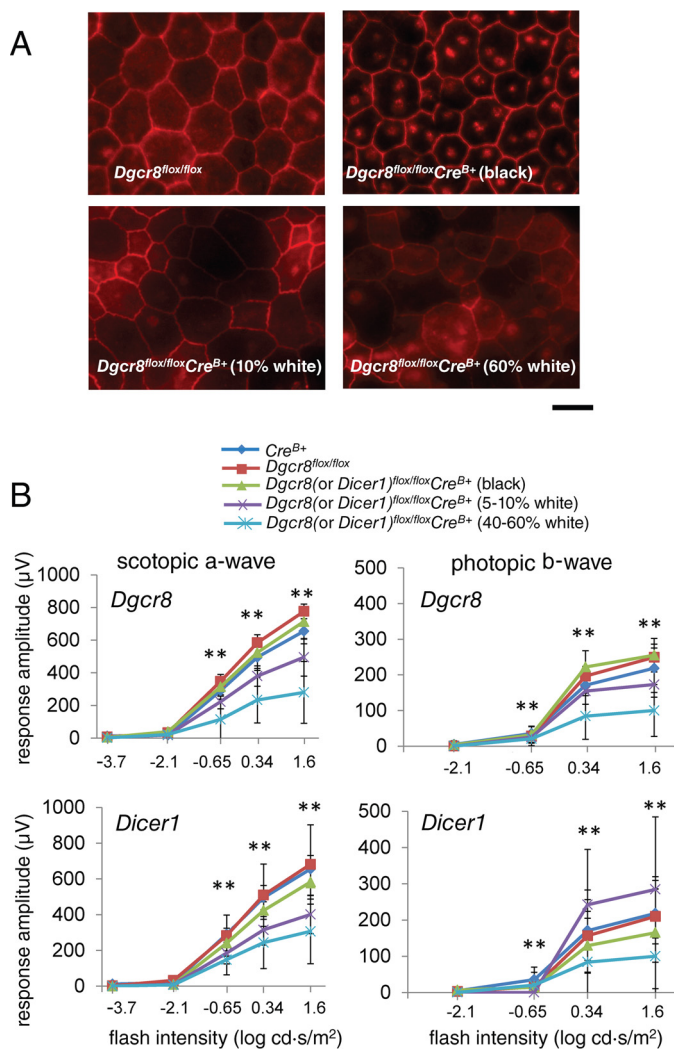
FIGURE 7. **Constitutive $Dgcr8^{flox/flox}Cre^{B+}$ mice exhibit defects in RPE monolayer integrity and visual function.** *A*, immunostaining of flat mounted RPE for the tight junction protein ZO-1 revealed a disruption of RPE organization in 8-week-old $Dgcr8^{flox/flox}Cre^{B+}$ mice proportional to their amount of white fur. *Scale bar*, 50 μm. *B*, ERG recordings revealed decreased amplitudes for both scotopic a-waves and photopic b-waves in $Dicer1^{flox/flox}Cre^{B+}$ and $Dgcr8^{flox/flox}Cre^{B+}$ mice with a high proportion of white fur. *p* values were statistically significant when calculated for $Dgcr8^{flox/flox}Cre^{B+}$ (5–10%) *versus* $Dgcr8^{flox/flox}$, $Dgcr8^{flox/flox}Cre^{B+}$ (40–60%) *versus* $Dgcr8^{flox/flox}$; *, $p < 0.001$ for $Dicer1^{flox/flox}Cre^{B+}$ (40–60%) *versus* Cre^{B+}, $Dgcr8^{flox/flox}Cre^{B+}$ *versus* Cre^{B+}, and $Dgcr8^{flox/flox}Cre^{B+}$ *versus* Cre^{B+}; $Dicer1^{flox/flox}Cre^{B+}$ (black) *versus* $Dicer1^{flox/flox}$, $Dicer1^{flox/flox}Cre^{B+}$ (black) *versus* Cre^{B+}, $Dicer1^{flox/flox}Cre^{B+}$ (5–10%) *versus* Cre^{B+}, $Dgcr8^{flox/flox}Cre^{B+}$ (black) *versus* $Dgcr8^{flox/flox}$, and $Dgcr8^{flox/flox}Cre^{B+}$ *versus* Cre^{B+}, $Dicer1^{flox/flox}Cre^{B+}$ (5–10%) *versus* $Dicer1^{flox/flox}$, $Dicer1^{flox/flox}Cre^{B+}$ (40–60%) *versus* $Dicer1^{flox/flox}$.

DROSHA and DGCR8 failed to result in RPE cell death observed upon delivery of the same cassette to $Dicer1^{flox/flox}$ mice (31). This result, combined with a lack of RPE morphological changes upon loss of any of the four mammalian Argonaute (AGO) family proteins involved in RNA silencing processes or of the RISC-loading complex subunit TARBP, indicated that RPE dysfunction in the absence of DICER1 is miRNA-independent. Hence, the results of our more systematic assessment of DGCR8 loss over a longer time course contrast with those findings reported previously (30). The impact of miRNA loss on mature RPE could be masked by more rapid cell death resulting from toxic SINE transcript accumulation in the absence of

DICER1 (52). Alternatively, the timing or efficacy of gene excision, decay of existing protein, or loss of mature miRNAs could differ dramatically between virus-driven *Dicer1* disruption and that of other factors associated with the miRNA response. For example, although expression of *Cre* recombinase began at postnatal day 6 in cone photoreceptor-specific *Dgcr8* cKO mice, significant loss of Dgcr8 protein was not obvious until postnatal day 60 (20). If protein components of the nuclear microprocessor complex are similarly stable in RPE cells, this would complicate the interpretation of results gleaned from comparing the effect of exogenous *Cre* recombinase delivery to mouse lines carrying different conditional alleles, especially when RPE morphology is assessed at a single post-injection time point. Also, due to the well documented functional redundancy of the four mammalian Argonaute family proteins to the miRNA response, individual disruption of either of these factors would not be expected to yield consequences as severe as those resulting from removal of DICER1, even if the loss of miRNAs were exclusively responsible for the phenotypic defects.

Further research must provide more detailed quantification of the miRNA and, most importantly, the resulting changes in mRNA. Challenges necessary to overcome include (i) the fact that deletion of DGCR8/DICER1 from monolayer of the retina is on the background of expression of the same miRNA in the neuronal retina and (ii) mosaic expression of *Cre* in the RPE, as demonstrated in the present study. The new study also will require additional genetic models and techniques.

Taken together, the results of the current investigation clearly demonstrate that DGCR8 is essential for the survival and function of mature RPE cells and adjacent photoreceptors in mice. This finding strongly suggests a fundamental loss of miRNA gene regulation in the mechanism of RPE dysfunction in the absence of DICER1. Because DICER1 depletion is a hallmark of GA, these results also implicate RPE miRNAs in the pathological progression of dry AMD and motivate a search for RPE miRNAs that could serve as biomarkers of disease progression or targets for novel interventions for this currently untreatable retinal degenerative disorder.

Materials and Methods

Animals—All animal procedures were approved by the Case Western Reserve University Animal Care and Use Committee. $Dicer1^{flox/flox}$ (39) and $Dgcr8^{flox/flox}$ (38) mice were purchased from Jackson Laboratory (Bar Harbor, ME). Inducible pVMAD2-rtTA-TRE-*Cre* (40) and non-inducible *BEST1-Cre* line (41) mature RPE cell-specific *Cre* mice were kind gifts from Yun Le (University of Oklahoma Health Sciences Center) and Joshua Dunaief (University of Pennsylvania), respectively. cKO animals were maintained by crossing conditional KO animals with cKO animals to generate 50% cKO progeny and 50% LoxP controls ($Dicer1^{flox/flox}Cre^{-}$ or $Dgcr8^{flox/flox}Cre^{-}$). Thus, all experiments were performed with littermate control animals. *Cre* control animals ($Dicer1^{+/+}Cre^{+}$ or $Dgcr8^{+/+}Cre^{+}$) were generated by crosses with C57BL/6J wild-type mice (Jackson Laboratory). Genotyping was performed as described previously (38–41). It should be noted that *Cre* expression is leaky,

≋ASBMB

arising from the inducible allele, such that *Cre* expression does not vary significantly between induced and uninduced animals. For mice carrying the inducible mature RPE cell-specific *Cre* transgene, expression was induced at postnatal day 21 by intraperitoneal injection of 100 μl of 10 mg/ml doxycycline in PBS (136 mM NaCl, 2 mM KCl, 8 mM Na$_2$HPO$_4$, 1 mM KH$_2$PO$_4$, pH 7.4) on two sequential days. However, a problem with the parental *Cre*$^{v+}$ line is that *Cre* expression is leaky, arising from the inducible allele, and therefore that *Cre* expression does not vary significantly between induced and uninduced animals. Animals were housed at the animal resource center at Case Western Reserve University School of Medicine, where they were maintained on a 12-h light ($\sim$10 lux)/12-h dark cycle and fed a normal chow diet.

Morphological and Functional Studies—SD-OCT was performed as described previously (19). For quantification, ONL thickness measurements were made 0.45 mm from the optic nerve head in the nasal, temporal, inferior, and superior direction of each eye, for a total of eight measurements per mouse. Data are presented as the means and S.D. of the averages of these eight measurements for at least five mice. For histology, mice were euthanized by CO$_2$ asphyxiation, and their eyes were removed and fixed for 48 h at room temperature in Hartmann's fixative (Sigma-Aldrich). Tissue processing, paraffin embedding, immunostaining, and quantification were performed as noted previously (19). For lower magnification images, 24-bit color images were captured at ×20 with an Olympus BX-60 upright microscope attached to a Retiga EXi camera (QImaging, Surrey, Canada). Acquisition and processing of images were done with Metamorph Imaging Software (Molecular Devices, Downingtown, PA). For higher magnification images, paraffin sections were imaged with an upright microscope (LeicaDM 6000 B, Leica Microsystems Inc., Wetzlar, Germany) equipped with a CCD color camera (Micropublisher version 5.0 RTV, QImaging) and Image-Pro software (Media Cybernetics, Rockville, MD). Images were analyzed with Adobe Photoshop (Adobe Systems Inc., San Jose, CA). To define the phenotype of 8-week-old *Dgcr8* cKO and control mice, retinal sections were prepared from six *Dgcr8*$^{flox/flox}$*Cre*$^{v+}$ mice, four *Cre* control mice, and two *Dgcr8*$^{flox/flox}$ control mice. In total, 66 sections were analyzed (28 sections from *Dgcr8*$^{flox/flox}$*Cre*$^{v+}$ mice, 15 from *Dgcr8*$^{flox/flox}$ mice, and 23 from *Cre* control mice). To observe the phenotypic details of photoreceptors and RPE cells, we imaged retinas with an HCX PL Fluotar ×100/1.30 NA oil lens (Leica Microsystems Inc.). Phenotypes of photoreceptor and RPE cells also were characterized at an earlier stage (5 weeks of age). A total of 11 mice (5 *Dgcr8*$^{flox/flox}$*Cre*$^{v+}$ and 6 *Dgcr8*$^{flox/flox}$ control mice) were analyzed. Experimenters were blinded to ensure unbiased interpretation of the data. To image retinal structures in an unbiased manner, two defined regions located at the middle between the ciliary marginal zone and the center of the retina were imaged with an HCX PL Fluotar ×100/1.30 NA oil lens. Likewise, other retinal regions were imaged where variable degrees of degeneration were discernible. With modifications, quantification of RPE phagocytosis was performed as described previously (53). Briefly, slides were incubated with xylene to remove paraffin and subjected to immunohistochemistry with a monoclonal antibody, B6-30

(54), that recognized the N terminus of rod opsin. The stained foci in regions representing at least 100 μm were counted, and the phagosomes per 100 μm were calculated. Three slides per eye were stained, two measurements were taken per eye, and two eyes were studied per animal, for a total of 12 measurements/animal. Quantitative data presented represent the means and S.D. of the averages of these 12 measurements for at least five animals per genotype and time point. Image stacks were collected in 0.2-μm steps in 14 bits on a Leica DMI 6000 B inverted microscope with a ×63 objective (1.4 NA Plan Apo) connected to a Retiga EXi Aqua camera. Metamorph Imaging software (Molecular Devices) was used for both acquisition and production of maximal projection images to discern the phagosomes.

For RFM, eyes of 8-week-old animals were isolated and the RPE attached to choroid-sclera was flat mounted on a dissecting microscope. RFMs were placed on a glass slide and fixed with 4% paraformaldehyde (Electron Microscopy Sciences, Hatfield, PA) in PBS for 15 min followed by washing twice in PBST (PBS containing 0.05% Tween). RFMs were incubated with PBST for 10 min, blocked with 10% goat serum (Sigma-Aldrich) in PBST for 5 min at room temperature. RFMs were incubated with primary antibody (rabbit polyclonal antibody against ZO-1; Invitrogen) (dilution 1:100) overnight at 4 °C in a moist chamber. RFMs were then washed with PBST three times for 10 min. After these washes, the RFMs were incubated with secondary antibody (Alexa Fluor 647-conjugated AffiniPure goat anti-rabbit IgG; Jackson ImmunoResearch Laboratories Inc., West Grove, PA) (1:200) for 2 h at room temperature in a moist chamber. The RFMs were washed three times for 10 min in PBST, followed by two 5-min washes with PBS. Washed RFMs were transferred to a new slide, mounted in 50% glycerol medium, and covered with a glass coverslip sealed with clear nail polish (Electron Microscopy Science). These RFMs were imaged by florescence microscopy on a Leica DMI 6000 B inverted microscope (NA 1.4 Plan Apo) connected to a Retiga EXi Aqua camera. Metamorph Imaging software was used for image acquisition.

ERG recordings were performed as described previously (19). Data represent the means and S.D. of the scotopic *a*-wave or photopic *b*-wave amplitudes derived from measurements of at least 5 animals/genotype.

HPLC-based quantification of the rate of recovery of 11-*cis*-retinal was performed as reported previously (55). Quantitative data represent the means and S.D. of measurements from 4–6 animals/genotype per time point.

For quantitative RT-PCR, total RNA derived from the isolated RPE/choroid of 8-week-old animals was used to create cDNA with the quantiTect® reverse transcription kit (Qiagen, Hilden, Germany). RT-PCR was performed with the Faststart Universal SYBR Green Master mix (Rox) (Roche Applied Science). *Gapdh* gene expression was used for normalization. The primer sequences were as follows: mGapdh-F, 5′-gtgttc-ctacccccaatgtg-3′ and mGapdh-R, 5′-ggagacaacctggtcctcag-3′; CreRT-F, 5′-taaactggtcgagcgatgga-3′ and CreRT-R, 5′-acc-agagtcatccttagcgc-3′.

Ultrastructural Studies—Plastic sections prepared from four *Dgcr8Cre*$^{v+}$ mice and one *Dgcr8*$^{flox/flox}$ control mouse were analyzed by TEM at 5 weeks of age. Fixation, sectioning, and staining were performed according to Sakami *et al.* (56). Briefly,

mouse eye cups were fixed with 2% formaldehyde and 2.5% glutaraldehyde and then cut in half with a blade. Cut eye cups were further fixed with the same solution and post-fixed with ferrocyanide-reduced osmium tetroxide. Then cut eye cups were stained with 0.25% uranyl acetate, dehydrated with a series of increasing concentrations of ethanol and propylene oxide, and infiltrated with epoxy resin. Cut eye cups were divided into two groups. The first group of cut eye cups was simply polymerized at 60 °C for 4.5 days. To enhance the infiltration of epoxy resin into pigmented granules of the RPE, the second group of cut eye cups were incubated with epoxy resin at 37 °C for 1 day and then polymerized at 60 °C for 2 days. The resulting plastic blocks containing cut eye cups were first sectioned at 400 or 600 nm with an ultramicrotome (MT6000-XL, RMC, Inc., Tucson, AZ). These sections were stained with Toluidine Blue O and observed by light microscopy. Then plastic blocks were trimmed to a small size and sectioned at ~80 nm. Thin plastic sections were placed on Formvar supporting membranes on 100-mesh grids. After staining and carbon coating, the ultrastructure of RPE and photoreceptor outer segments was analyzed with TEM (Tecnai F20, FEI, Hillsboro, OR) at 200 kV. TEM images were obtained with a CMOS camera (TemCam-F416, TVIPS, Gauting, Germany) and EM-MENU software (TVIPS).

Statistical Analyses—Data representing the means ± S.D. for the results of at least three independent experiments were compared by one-way analysis of variance with a p value of <0.05 considered statistically significant.

References

1. Wong, W. L., Su, X., Li, X., Cheung, C. M., Klein, R., Cheng, C. Y., and Wong, T. Y. (2014) Global prevalence of age-related macular degeneration and disease burden projection for 2020 and 2040: a systematic review and meta-analysis. *Lancet Glob. Health* **2,** e106–116

2. Chappelow, A. V., and Kaiser, P. K. (2008) Neovascular age-related macular degeneration: potential therapies. *Drugs* **68,** 1029–1036

3. Ambati, J. (2011) Age-related macular degeneration and the other double helix: the Cogan lecture. *Invest. Ophthalmol. Vis. Sci.* **52,** 2165–2169

4. Chen, Y., Bedell, M., and Zhang, K. (2010) Age-related macular degeneration: genetic and environmental factors of disease. *Mol. Interv.* **10,** 271–281

5. Yazdi, M. H., Faramarzi, M. A., Nikfar, S., Falavarjani, K. G., and Abdollahi, M. (2015) Ranibizumab and aflibercept for the treatment of wet age-related macular degeneration. *Expert Opin. Biol. Ther.* **15,** 1349–1358

6. Peden, M. C., Suñer, I. J., Hammer, M. E., and Grizzard, W. S. (2015) Long-term outcomes in eyes receiving fixed-interval dosing of anti-vascular endothelial growth factor agents for wet age-related macular degeneration. *Ophthalmology* **122,** 803–808

7. Ambati, J., and Fowler, B. J. (2012) Mechanisms of age-related macular degeneration. *Neuron* **75,** 26–39

8. Rofagha, S., Bhisitkul, R. B., Boyer, D. S., Sadda, S. R., Zhang, K., and SEVEN-UP Study Group (2013) Seven-year outcomes in ranibizumab-treated patients in ANCHOR, MARINA, and HORIZON: a multicenter cohort study (SEVEN-UP). *Ophthalmology* **120,** 2292–2299

9. Nowak, J. Z. (2006) Age-related macular degeneration (AMD): pathogenesis and therapy. *Pharmacol. Rep.* **58,** 353–363

10. Cheung, L. K., and Eaton, A. (2013) Age-related macular degeneration. *Pharmacotherapy* **33,** 838–855

11. Kleinman, M. E., and Ambati, J. (2016) Complement activation and inhibition in retinal diseases. *Dev. Ophthalmol.* **55,** 46–56

12. Lee, R. C., Feinbaum, R. L., and Ambros, V. (1993) The *C. elegans* heterochronic gene *lin-4* encodes small RNAs with antisense complementarity to *lin-14*. *Cell* **75,** 843–854

13. Wightman, B., Ha, I., and Ruvkun, G. (1993) Posttranscriptional regulation of the heterochronic gene *lin-14* by *lin-4* mediates temporal pattern formation in *C. elegans*. *Cell* **75,** 855–862

14. Fabian, M. R., Sundermeier, T. R., and Sonenberg, N. (2010) Understanding how miRNAs post-transcriptionally regulate gene expression. *Prog. Mol. Subcell. Biol.* **50,** 1–20

15. Leung, A. K., and Sharp, P. A. (2010) MicroRNA functions in stress responses. *Mol. Cell* **40,** 205–215

16. Peláez, N., and Carthew, R. W. (2012) Biological robustness and the role of microRNAs: a network perspective. *Curr. Top. Dev. Biol.* **99,** 237–255

17. Emde, A., and Hornstein, E. (2014) miRNAs at the interface of cellular stress and disease. *EMBO J.* **33,** 1428–1437

18. Vidigal, J. A., and Ventura, A. (2015) The biological functions of miRNAs: lessons from *in vivo* studies. *Trends Cell Biol.* **25,** 137–147

19. Sundermeier, T. R., Zhang, N., Vinberg, F., Mustafi, D., Kohno, H., Golczak, M., Bai, X., Maeda, A., Kefalov, V. J., and Palczewski, K. (2014) DICER1 is essential for survival of postmitotic rod photoreceptor cells in mice. *FASEB J.* **28,** 3780–3791

20. Busskamp, V., Krol, J., Nelidova, D., Daum, J., Szikra, T., Tsuda, B., Jüttner, J., Farrow, K., Scherf, B. G., Alvarez, C. P., Genoud, C., Sothilingam, V., Tanimoto, N., Stadler, M., Seeliger, M., *et al.* (2014) miRNAs 182 and 183 are necessary to maintain adult cone photoreceptor outer segments and visual function. *Neuron* **83,** 586–600

21. Zhu, Q., Sun, W., Okano, K., Chen, Y., Zhang, N., Maeda, T., and Palczewski, K. (2011) Sponge transgenic mouse model reveals important roles for the microRNA-183/96/182 cluster in postmitotic photoreceptors of the retina. *J. Biol. Chem.* **286,** 31749–31760

22. Lumayag, S., Haldin, C. E., Corbett, N. J., Wahlin, K. J., Cowan, C., Turturro, S., Larsen, P. E., Kovacs, B., Witmer, P. D., Valle, D., Zack, D. J., Nicholson, D. A., and Xu, S. (2013) Inactivation of the microRNA-183/96/182 cluster results in syndromic retinal degeneration. *Proc. Natl. Acad. Sci. U.S.A.* **110,** E507–E516

23. Krol, J., Krol, I., Alvarez, C. P., Fiscella, M., Hierlemann, A., Roska, B., and Filipowicz, W. (2015) A network comprising short and long noncoding RNAs and RNA helicase controls mouse retina architecture. *Nat. Commun.* **6,** 7305

24. Sundermeier, T. R., and Palczewski, K. (2016) The impact of microRNA gene regulation on the survival and function of mature cell types in the eye. *FASEB J.* **30,** 23–33

25. Young, R. W., and Bok, D. (1969) Participation of the retinal pigment epithelium in the rod outer segment renewal process. *J. Cell Biol.* **42,** 392–403

26. McBee, J. K., Palczewski, K., Baehr, W., and Pepperberg, D. R. (2001) Confronting complexity: the interlink of phototransduction and retinoid metabolism in the vertebrate retina. *Prog. Retin. Eye Res.* **20,** 469–529

27. Kevany, B. M., and Palczewski, K. (2010) Phagocytosis of retinal rod and cone photoreceptors. *Physiology* **25,** 8–15

28. Adijanto, J., Castorino, J. J., Wang, Z. X., Maminishkis, A., Grunwald, G. B., and Philp, N. J. (2012) Microphthalmia-associated transcription factor (MITF) promotes differentiation of human retinal pigment epithelium (RPE) by regulating microRNAs-204/211 expression. *J. Biol. Chem.* **287,** 20491–20503

29. Wang, F. E., Zhang, C., Maminishkis, A., Dong, L., Zhi, C., Li, R., Zhao, J., Majerciak, V., Gaur, A. B., Chen, S., and Miller, S. S. (2010) MicroRNA-204/211 alters epithelial physiology. *FASEB J.* **24,** 1552–1571

30. Ohana, R., Weiman-Kelman, B., Raviv, S., Tamm, E. R., Pasmanik-Chor, M., Rinon, A., Netanely, D., Shamir, R., Solomon, A. S., and Ashery-Padan, R. (2015) MicroRNAs are essential for differentiation of the retinal pigmented epithelium and maturation of adjacent photoreceptors. *Development* **142,** 2487–2498

31. Kaneko, H., Dridi, S., Tarallo, V., Gelfand, B. D., Fowler, B. J., Cho, W. G., Kleinman, M. E., Ponicsan, S. L., Hauswirth, W. W., Chiodo, V. A., Karikó, K., Yoo, J. W., Lee, D. K., Hadziahmetovic, M., Song, Y., *et al.* (2011) DICER1 deficit induces Alu RNA toxicity in age-related macular degeneration. *Nature* **471,** 325–330

32. Gelfand, B. D., Wright, C. B., Kim, Y., Yasuma, T., Yasuma, R., Li, S., Fowler, B. J., Bastos-Carvalho, A., Kerur, N., Uittenbogaard, A., Han, Y. S., Lou, D., Kleinman, M. E., McDonald, W. H., Núñez, G., *et al.* (2015) Iron toxicity in the retina requires Alu RNA and the NLRP3 inflammasome. *Cell Rep.* **11,** 1686–1693

33. Fowler, B. J., Gelfand, B. D., Kim, Y., Kerur, N., Tarallo, V., Hirano, Y., Amarnath, S., Fowler, D. H., Radwan, M., Young, M. T., Pittman, K., Kubes, P., Agarwal, H. K., Parang, K., Hinton, D. R., *et al.* (2014) Nucleoside reverse transcriptase inhibitors possess intrinsic anti-inflammatory activity. *Science* **346,** 1000–1003

34. Kim, Y., Tarallo, V., Kerur, N., Yasuma, T., Gelfand, B. D., Bastos-Carvalho, A., Hirano, Y., Yasuma, R., Mizutani, T., Fowler, B. J., Li, S., Kaneko, H., Bogdanovich, S., Ambati, B. K., Hinton, D. R., *et al.* (2014) DICER1/Alu RNA dysmetabolism induces caspase-8-mediated cell death in age-related macular degeneration. *Proc. Natl. Acad. Sci. U.S.A.* **111,** 16082–16087

35. Kerur, N., Hirano, Y., Tarallo, V., Fowler, B. J., Bastos-Carvalho, A., Yasuma, T., Yasuma, R., Kim, Y., Hinton, D. R., Kirschning, C. J., Gelfand, B. D., and Ambati, J. (2013) TLR-independent and P2X7-dependent signaling mediate Alu RNA-induced NLRP3 inflammasome activation in geographic atrophy. *Invest. Ophthalmol. Vis. Sci.* **54,** 7395–7401

36. Dridi, S., Hirano, Y., Tarallo, V., Kim, Y., Fowler, B. J., Ambati, B. K., Bogdanovich, S., Chiodo, V. A., Hauswirth, W. W., Kugel, J. F., Goodrich, J. A., Ponicsan, S. L., Hinton, D. R., Kleinman, M. E., Baffi, J. Z., *et al.* (2012) ERK1/2 activation is a therapeutic target in age-related macular degeneration. *Proc. Natl. Acad. Sci. U.S.A.* **109,** 13781–13786

37. Tarallo, V., Hirano, Y., Gelfand, B. D., Dridi, S., Kerur, N., Kim, Y., Cho, W. G., Kaneko, H., Fowler, B. J., Bogdanovich, S., Albuquerque, R. J., Hauswirth, W. W., Chiodo, V. A., Kugel, J. F., Goodrich, J. A., *et al.* (2012) DICER1 loss and Alu RNA induce age-related macular degeneration via the NLRP3 inflammasome and MyD88. *Cell* **149,** 847–859

38. Rao, P. K., Toyama, Y., Chiang, H. R., Gupta, S., Bauer, M., Medvid, R., Reinhardt, F., Liao, R., Krieger, M., Jaenisch, R., Lodish, H. F., and Blelloch, R. (2009) Loss of cardiac microRNA-mediated regulation leads to dilated cardiomyopathy and heart failure. *Circ. Res.* **105,** 585–594

39. Harfe, B. D., McManus, M. T., Mansfield, J. H., Hornstein, E., and Tabin, C. J. (2005) The RNaseIII enzyme Dicer is required for morphogenesis but not patterning of the vertebrate limb. *Proc. Natl. Acad. Sci. U.S.A.* **102,** 10898–10903

40. Le, Y. Z., Zheng, W., Rao, P. C., Zheng, L., Anderson, R. E., Esumi, N., Zack, D. J., and Zhu, M. (2008) Inducible expression of cre recombinase in the retinal pigmented epithelium. *Invest. Ophthalmol. Vis. Sci.* **49,** 1248–1253

41. Iacovelli, J., Zhao, C., Wolkow, N., Veldman, P., Gollomp, K., Ojha, P., Lukinova, N., King, A., Feiner, L., Esumi, N., Zack, D. J., Pierce, E. A., Vollrath, D., and Dunaief, J. L. (2011) Generation of Cre transgenic mice with postnatal RPE-specific ocular expression. *Invest. Ophthalmol. Vis. Sci.* **52,** 1378–1383

42. Marmorstein, A. D., Marmorstein, L. Y., Rayborn, M., Wang, X., Hollyfield, J. G., and Petrukhin, K. (2000) Bestrophin, the product of the Best vitelliform macular dystrophy gene (VMD2), localizes to the basolateral plasma membrane of the retinal pigment epithelium. *Proc. Natl. Acad. Sci. U.S.A.* **97,** 12758–12763

43. Staurenghi, G., Sadda, S., Chakravarthy, U., Spaide, R. F., and International Nomenclature for Optical Coherence Tomography (IN·OCT) Panel (2014) Proposed lexicon for anatomic landmarks in normal posterior segment spectral-domain optical coherence tomography: the IN*OCT consensus. *Ophthalmology* **121,** 1572–1578

44. Yaqoob, Z., Wu, J., and Yang, C. (2005) Spectral domain optical coherence tomography: a better OCT imaging strategy. *BioTechniques* **39,** S6–S13

45. Robison, W. G., Jr., and Kuwabara, T. (1977) Vitamin A storage and peroxisomes in retinal pigment epithelium and liver. *Invest. Ophthalmol. Vis. Sci.* **16,** 1110–1117

46. Tauchi-Sato, K., Ozeki, S., Houjou, T., Taguchi, R., and Fujimoto, T. (2002) The surface of lipid droplets is a phospholipid monolayer with a unique fatty acid composition. *J. Biol. Chem.* **277,** 44507–44512

47. Mione, M., and Bosserhoff, A. (2015) MicroRNAs in melanocyte and melanoma biology. *Pigment Cell Melanoma Res.* **28,** 340–354

48. Dai, X., Rao, C., Li, H., Chen, Y., Fan, L., Geng, H., Li, S., Qu, J., and Hou, L. (2015) Regulation of pigmentation by microRNAs: MITF-dependent microRNA-211 targets TGF-β receptor 2. *Pigment Cell Melanoma Res.* **28,** 217–222

49. Jian, Q., An, Q., Zhu, D., Hui, K., Liu, Y., Chi, S., and Li, C. (2014) MicroRNA 340 is involved in UVB-induced dendrite formation through the regulation of RhoA expression in melanocytes. *Mol. Cell. Biol.* **34,** 3407–3420

50. Dynoodt, P., Mestdagh, P., Van Peer, G., Vandesompele, J., Goossens, K., Peelman, L. J., Geusens, B., Speeckaert, R. M., Lambert, J. L., and Van Gele, M. J. (2013) Identification of miR-145 as a key regulator of the pigmentary process. *J. Invest. Dermatol.* **133,** 201–209

51. Dong, C., Wang, H., Xue, L., Dong, Y., Yang, L., Fan, R., Yu, X., Tian, X., Ma, S., and Smith, G. W. (2012) Coat color determination by miR-137 mediated down-regulation of microphthalmia-associated transcription factor in a mouse model. *RNA* **18,** 1679–1686

52. Tajaddod, M., Tanzer, A., Licht, K., Wolfinger, M. T., Badelt, S., Huber, F., Pusch, O., Schopoff, S., Janisiw, M., Hofacker, I., and Jantsch, M. F. (2016) Transcriptome-wide effects of inverted SINEs on gene expression and their impact on RNA polymerase II activity. *Genome Biol.* **17,** 220

53. Sethna, S., and Finnemann, S. C. (2013) Analysis of photoreceptor rod outer segment phagocytosis by RPE cells *in situ. Methods Mol. Biol.* **935,** 245–254

54. Adamus, G., Zam, Z. S., Arendt, A., Palczewski, K., McDowell, J. H., and Hargrave, P. A. (1991) Anti-rhodopsin monoclonal antibodies of defined specificity: characterization and application. *Vision Res.* **31,** 17–31

55. Golczak, M., Bereta, G., Maeda, A., and Palczewski, K. (2010) Molecular biology and analytical chemistry methods used to probe the retinoid cycle. *Methods Mol. Biol.* **652,** 229–245

56. Sakami, S., Kolesnikov, A. V., Kefalov, V. J., and Palczewski, K. (2014) P23H opsin knock-in mice reveal a novel step in retinal rod disc morphogenesis. *Hum. Mol. Genet.* **23,** 1723–1741